



**HAL**  
open science

# Mechanical properties and microstructural study of homogeneous and heterogeneous laser welds in $\alpha$ , $\beta$ , and $\alpha + \beta$ titanium alloys

Laurent Weiss, Julien Zollinger, Pierre Sallamand, Eugen Cicala, Alexandre Mathieu, Eric Fleury

## ► To cite this version:

Laurent Weiss, Julien Zollinger, Pierre Sallamand, Eugen Cicala, Alexandre Mathieu, et al.. Mechanical properties and microstructural study of homogeneous and heterogeneous laser welds in  $\alpha$ ,  $\beta$ , and  $\alpha + \beta$  titanium alloys. *Welding in the World*, 2019, 63 (1), pp.53-62. 10.1007/s40194-018-0627-1 . hal-02455047

**HAL Id: hal-02455047**

**<https://hal.science/hal-02455047v1>**

Submitted on 25 Jan 2020

**HAL** is a multi-disciplinary open access archive for the deposit and dissemination of scientific research documents, whether they are published or not. The documents may come from teaching and research institutions in France or abroad, or from public or private research centers.

L'archive ouverte pluridisciplinaire **HAL**, est destinée au dépôt et à la diffusion de documents scientifiques de niveau recherche, publiés ou non, émanant des établissements d'enseignement et de recherche français ou étrangers, des laboratoires publics ou privés.

# Mechanical properties and microstructural study of homogeneous and heterogeneous laser welds in $\alpha$ , $\beta$ , and $\alpha + \beta$ titanium alloys

Laurent Weiss<sup>1,2</sup> · J. Zollinger<sup>2,3</sup> · P. Sallamand<sup>4</sup> · E. Cicala<sup>4</sup> · A. Mathieu<sup>4</sup> · E. Fleury<sup>1,2</sup>

Received: 6 September 2017 / Accepted: 7 July 2018

© International Institute of Welding 2018

## Abstract

Heterogeneous welding has been investigated for three different couples of titanium alloys:  $\alpha/\alpha + \beta$ ,  $\alpha/\beta$ , and  $\alpha + \beta/\beta$ . Plates of  $100 \times 60$  mm and 1.6 or 1.8 mm thick were welded with a Yb:YAG laser. Tensile tests show that the resistance of the heterogeneous welded specimens was generally controlled by those of the weakest material except for the  $\alpha + \beta/\beta$  where the ultimate tensile strength was approximately equal to the average value of both materials. In every case, the elongation of the welded sample was found to be smaller than that of the base metals. The rupture generally took place outside the weld metal and was found to be most of the time located in the alloy having the lowest mechanical properties. Nevertheless, a few large-size porosities detected by tomography in the  $\alpha + \beta/\beta$  couple could explain why rupture for these samples occurred in the weld bead. For each couple, the porosities were situated at the board between the heat-affected zone and the molten zone. EBSD maps and EDX enabled the observation of different microstructures, which could be correlated to the heterogeneous composition and diffusion into the melted bath. When the stable microstructure of one of the couple alloys is the  $\beta$  phase, the molten zone of the bead consists of an alternative disposition of thin layers made of large equiaxed  $\beta$  grains and nano-martensite  $\alpha'$ . That is explained by the weak diffusion of the alloying elements.

**Keywords** Titanium alloys · Laser welding · Heterogeneous joints · Microstructure · Mechanical properties

## 1 Introduction

The welding of titanium alloys has recently received much interests, particularly in aeronautics, and it is expected that welded components even of class 1 could be integrated in future commercial airplanes. In aviation, each part of the

components does not necessarily need to withstand the same mechanical stress, the same corrosive environment, or the same working temperature. Nevertheless, for standardization purposes, the pieces are made of the same alloy and are often oversized compared to the actual need. Some papers have reported studies about heterogeneous titanium welding such as Ti-Al [1, 2] Ti steel [3, 4], or Ti-Mg [5, 6] but a few only are dealing with welding of Ti alloys with different chemical compositions and microstructures. Wang et al. [7] have shown that heterogeneous electron beam welding (Ti-6Al-4V and BT9) was comprised of  $\alpha'$  martensite in the HAZ (heat-affected zone) and FZ (fusion zone) with properties close to the alloy with the lower mechanical properties. According to Ferdinand [8], for  $\beta$ -21S and Ti6242 alloys, the widths of welds prepared by laser were lower than those obtained by TIG welding, and the mechanical properties were found to be superior. To increase the knowledge, we have selected three different titanium alloys commonly used in aeronautics, each alloy having its own qualities: T50A (pure titanium) is the cheapest and has the best ductility, Ti-6Al-4V has an excellent mechanical strength/density ratio, and Ti-15Mo-3Al-2.7Nb-0.2Si (21S) is

✉ Laurent Weiss  
laurent.weiss@univ-lorraine.fr

<sup>1</sup> LEM3, Université de Lorraine, Ile du Saulcy, 57000 Metz, France

<sup>2</sup> Laboratory of Excellence for Design of Alloy Metals for Low-mass Structures ('DAMAS' Labex), Université de Lorraine, Metz, France

<sup>3</sup> Department of Metallurgy and Materials Science and Engineering, Institut Jean Lamour, Université de Lorraine, Parc de Saurupt, F-54011 Nancy, France

<sup>4</sup> Laboratoire Interdisciplinaire Carnot de Bourgogne, Université de Bourgogne, 12 rue de la fonderie, 71200 Le Creusot, France

the alloy having the greater resistance to oxidation/corrosion at high temperature. Their properties are the consequence of their different compositions and microstructures: pure  $\alpha$  for T50A,

$\alpha + \beta$  for Ti-6Al-4V, and pure  $\beta$  for 21S. These alloys were butt welded under various welding processing parameters using a Yb:YAG laser. An experimental design was defined

**Table 1** Tensile test results

Materials and welds	Power (kW)	Travel speed (m/min)	Beam offset (mm)	Maximum strength (MPa)	Elongation at maximum strength (%)	Elongation at break (%)	Young's modulus (GPa)
Raw T50A	–	–	–	432.3	10.1	62.2	93.2
Raw Ti21S	–	–	–	868.9	1.4	42.1	81.8
Raw TA6V	–	–	–	979.0	9.9	18.5	103.5
T50A/T50A	2.5	2.5	0	446.8	6.5	12.4	91.9
TA6V/TA6V	2.5	2.5	0	1016.5	5.9	7.6	101.1
21S/21S	2.5	2.5	0	862.6	2.4	29.2	62.2
T50A/TA6V	2.5	2.5	0	452.2	3.0	5.5	108.5
	2.5	2.5	–0.3	451.2	2.1	3.5	126.9
	2.5	2.5	0.3	447.8	2.7	5.8	114.6
	3	2	0.3	453.5	3.7	8.5	212.9
	2.5	2	0	446.8	2.5	4.0	100.2
	2	2	–0.3	451.9	3.3	6.3	143.5
	2	2.5	0	447.4	3.5	6.5	80.6
	3	2.5	–0.3	445.3	3.0	5.2	74.6
	3	3	0	449.0	2.8	5.5	123.2
	2.5	3	–0.3	455.0	2.6	4.8	126.7
	2	3	0.3	458.1	4.2	9.1	118.8
	3	2	0	451.2	2.3	3.4	92.7
T50A/21S	2.5	2.5	0	465.6	3.7	7.6	111.2
	2.5	2.5	–0.3	449.9	2.8	5.1	95.8
	2.5	2.5	0.3	445.9	2.9	5.1	92.0
	3	2	0.3	446.4	4.4	9.8	80.9
	2.5	2	0	449.7	2.7	4.9	96.5
	2	2	–0.3	454.0	3.1	5.4	86.4
	2	2.5	0	450.2	2.5	4.1	77.3
	3	2	0	451.6	2.3	3.9	123.6
	3	2.5	–0.3	451.2	2.9	5.2	98.5
	3	3	0	447.9	2.0	4.5	82.6
	2.5	3	–0.3	449.6	3.4	5.5	76.0
	2	3	0.3	451.7	4.7	10.4	80.8
	3	2	0	449.7	3.1	5.4	80.2
TA6V/21S	2.5	2.5	0	906.1	2.5	18.1	80.7
	2.5	2.5	–0.3	901.5	1.8	4.3	78.5
	2.5	2.5	0.3	893.5	1.9	6.4	79.9
	3	2	0.3	878.7	1.6	1.8	92.1
	2.5	2	0	875.6	1.8	2.0	71.6
	2	2	–0.3	910.1	1.6	4.6	76.5
	2	2.5	0	883.7	2.0	10.1	83.6
	3	2.5	–0.3	895.6	2.0	6.7	77.7
	3	3	0	889.2	2.3	7.0	74.2
	2.5	3	–0.3	904.1	1.6	10.2	73.7
	2	3	0.3	910.8	1.5	6.2	83.3
	3	2	0	836.5	1.9	3.8	69.0

based on variation of the parameters such as the travel speed ( $v$ ), power ( $P$ ), and the beam offset from the joint line ( $\Delta x$ ). The aims are to relate the change in the microstructure and properties to the processing conditions, and to propose procedures to improve the performance of the welded joints.

## 2 Materials and methods

Sheets of 1.6-, 1.8- and 1.83-mm thicknesses for the Ti50A, Ti-6Al-4V (further referred to as TA6V), and  $\beta$ -21S (referred as 21S), respectively, were purchased in the annealed state from TIMET Company. Those sheets were cut by water jet cutting to obtain  $60 \times 100$  mm rectangular plates, which were then butt welded to form three combinations: Ti50A/TA6V, Ti50A/21S, and TA6V/21S. Plates were cleaned with acetone before welding. The welding experiments were carried out in keyhole mode using a Yb:YAG laser (from TRUMPF) with a maximum beam power of 6 kW and a focused spot diameter of 600  $\mu\text{m}$ . The laser beam was focused on the top surface. Argon was used as top and bottom shielding gas with a flow rate of 20 L/min. Design of experiments was applied to study the effect of power (2, 2.5, and 3 kW), travel speed (2, 2.5, and 3 m/min), and beam offset from the joint line ( $-0.3, 0$ , and  $0.3$  mm). Preliminary tests were performed to find the suitable parameters and to limit the extent of the experimental design.

Tensile test specimens were extracted perpendicularly to the weld bead by means of water jet cutting to avoid thermal effects. The tensile test experiments were performed on the heterogeneous and homogeneous welded plates in the as-welded state and completed by tests on the unwelded alloys with an Instron tensile test machine using an initial strain rate of  $10^{-2} \text{ s}^{-1}$ . Volumetric internal weld imperfections were detected by tomography analyses using an EasyTom Nano Tomograph (RXSolutions) with a spatial resolution equal to 4  $\mu\text{m}$  when the studied bead length is 5 mm. The reconstructions were performed with XACT software. Nano-indentation was performed with a Berkovich tip ( $F = 100 \text{ mN}$  and  $v = 100 \text{ mN min}^{-1}$ ) and the hardness was measured using the Oliver and Pharr method [9].

The macrographic analysis was performed with an optical microscope Olympus BX61 and reconstruction multi-mapping with Stream Motion software. The SEM images were taken on two different scanning electron microscopes (SEM): a JEOL JSM-6490 (with a W gun emitter) and a Zeiss Supra 40 (with a Schottky field emission emitter). Grain orientations were determined by EBSD, using AZtech (Oxford Instruments, HKL Technology) for data acquisition and the chemical composition using EDX and Esprit Software (Brüker). Thermodynamic calculations were performed with the Thermo-Calc software using the commercial TTTi3 database [10] to determine the characteristic temperatures of the phase transformations.

## 3 Experimental results and discussion

The values given on Table 1 are the average of three tensile tests for each condition. For comparison, the stress-strain curves of the base materials under uniaxial tensile stress are

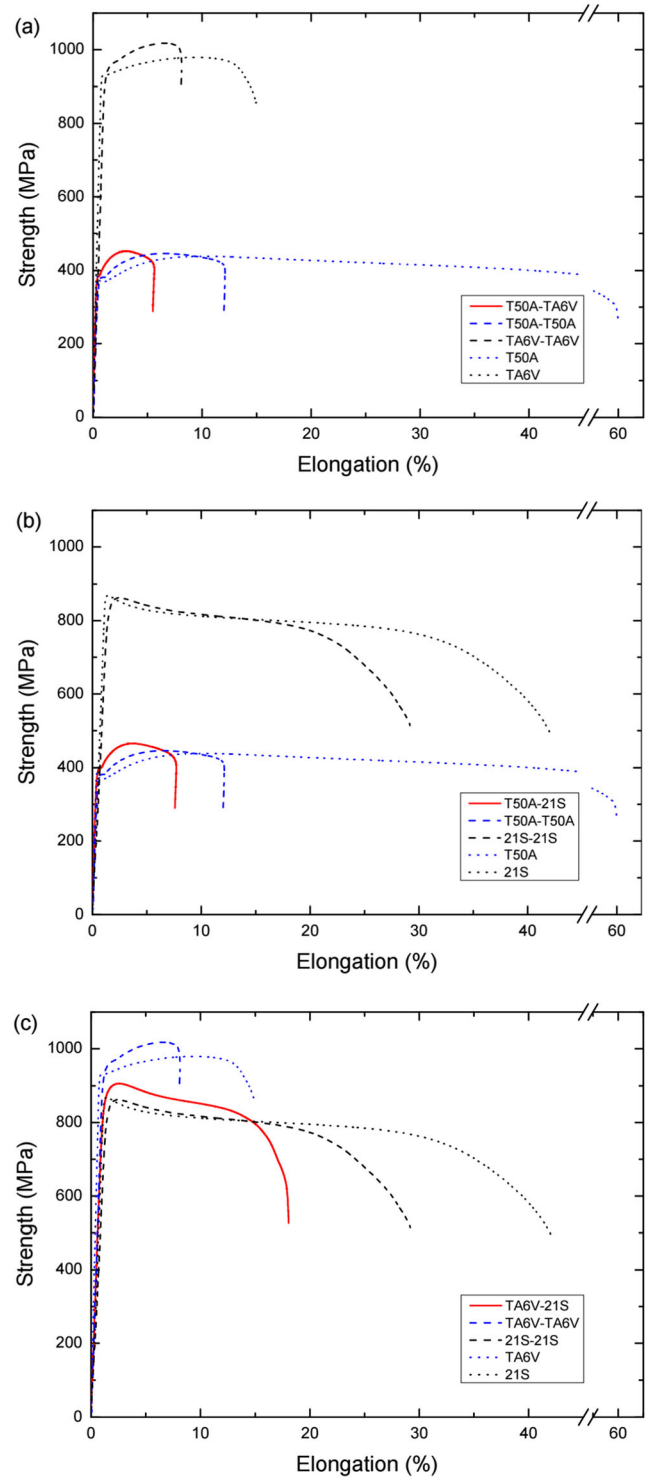
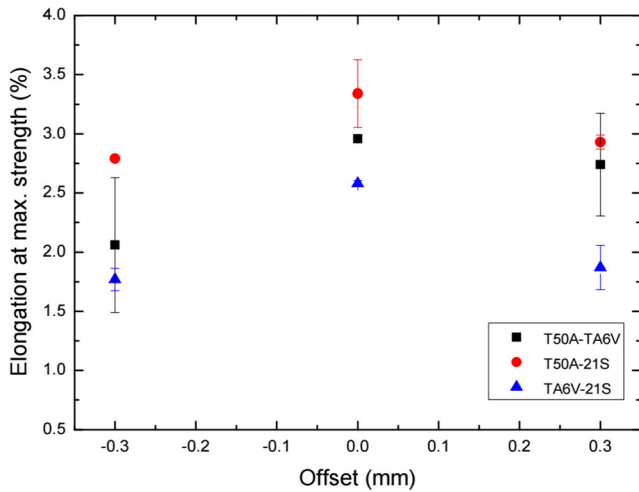
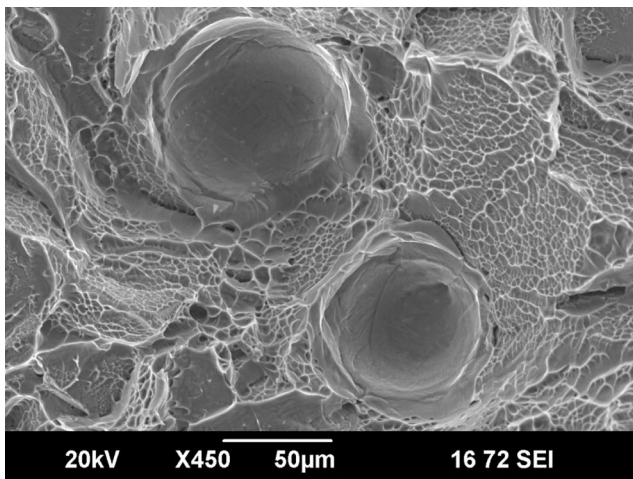


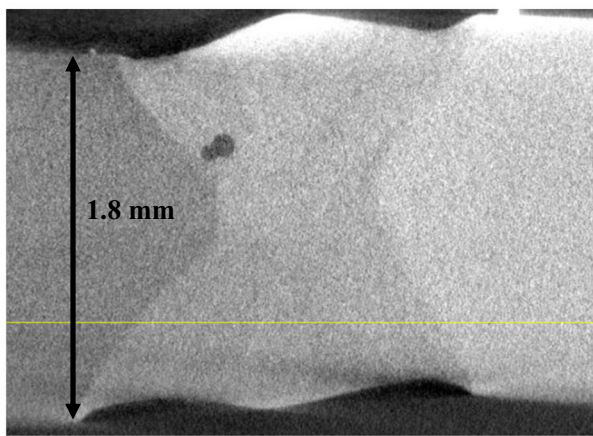
Fig. 1 Tensile tests ( $P = 2.5 \text{ kW}$ ,  $v = 2.5 \text{ m/min}$ ,  $\Delta x = 0$ ) of different couples with a T50A/TA6V, b T50A/21S, and c TA6V/21S [11]



**Fig. 2** Elongation at maximal strength as a function of beam offset from the joint line ( $P = 2.5$  kW and  $v = 2.5$  m/min) [11]



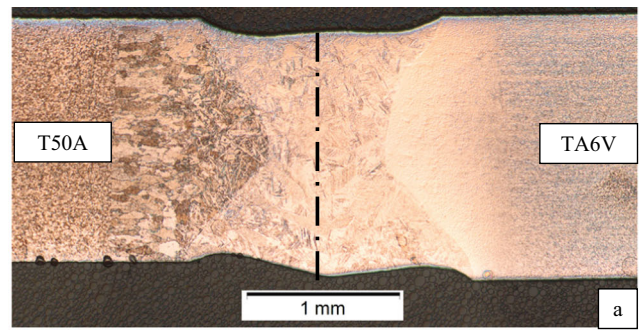
(a)



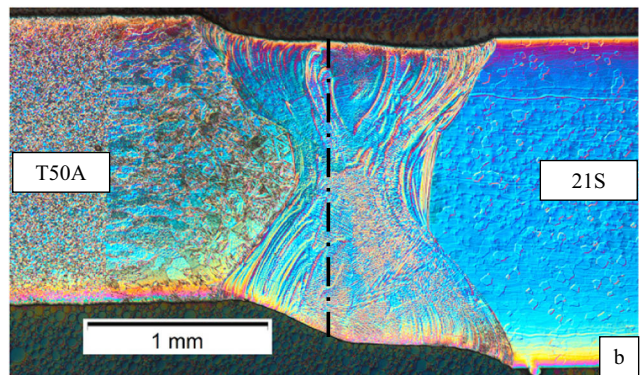
(b)

**Fig. 3** a SEM image of porosities at the fracture surface of TA6V/21S when the sample has broken in the bead. b X-ray tomography image of porosities in the TA6V/21S bead ( $P = 3$  kW,  $v = 3$  m/min, and  $\Delta x = 0$  mm) [11]

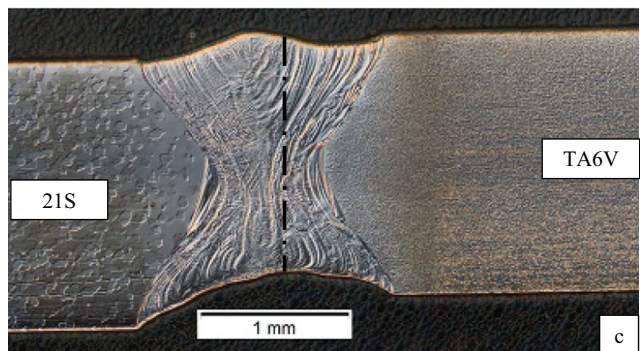
plotted in Fig. 1 together with those obtained for the heterogeneous welding assemblies. The T50A alloy displayed the largest elongation and the TA6V the highest ultimate tensile strength. Despite the characteristics of these base materials, the T50A/TA6V couple presented the lowest performance in terms of both strength and ductility. The hardening in the stress-strain curve and the elongation at fracture were comparable to those of TA6V/TA6V while the value of the ultimate tensile strength corresponded to that of the T50A. Similarly to that described above for the T50A/TA6V, the properties measured for the T50A/21S heterogeneous weld were also significantly reduced in comparison to those of the parent alloys. The form of the stress-strain curve for the T50A/21S heterogeneous weld was totally different than the 21S in the plastic zone. Nevertheless, we can note that the homogeneous 21S/21S couple preserved the characteristics of the 21S parent



a



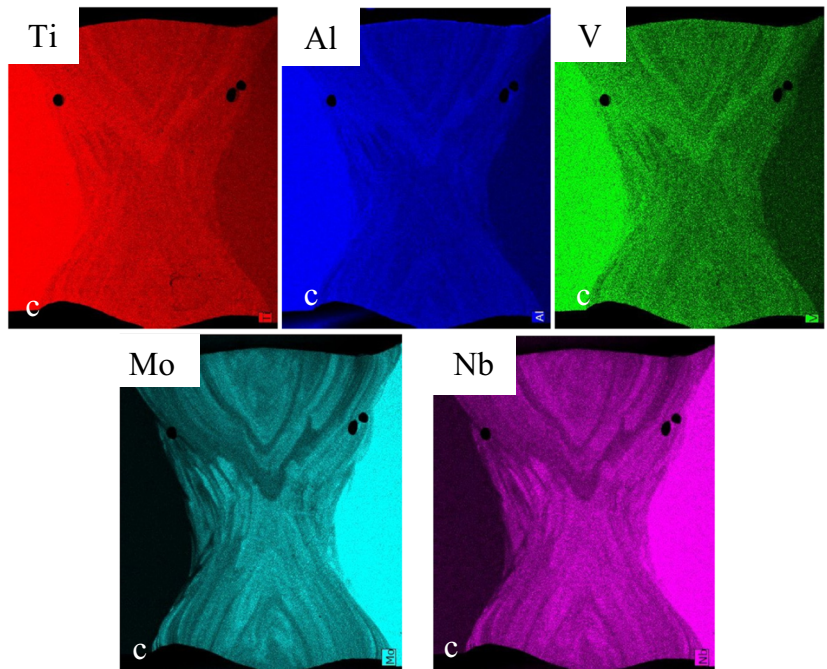
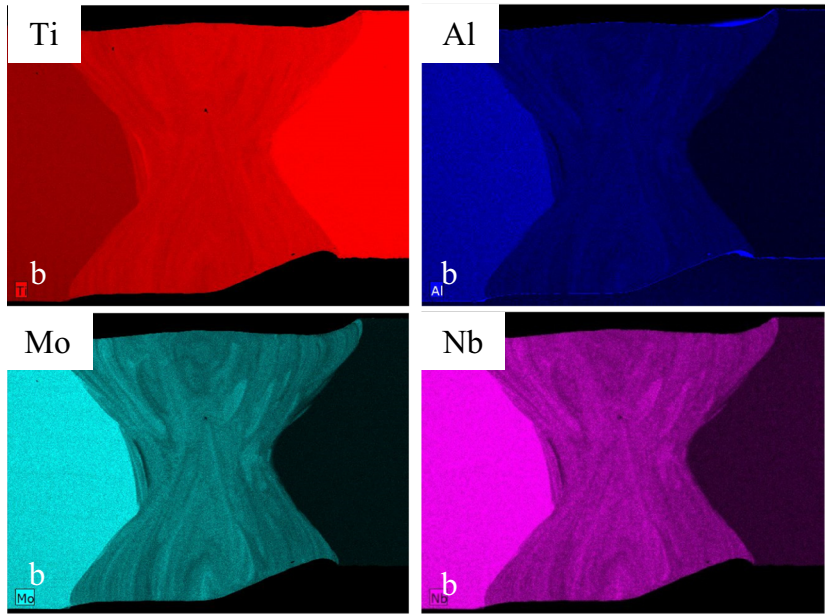
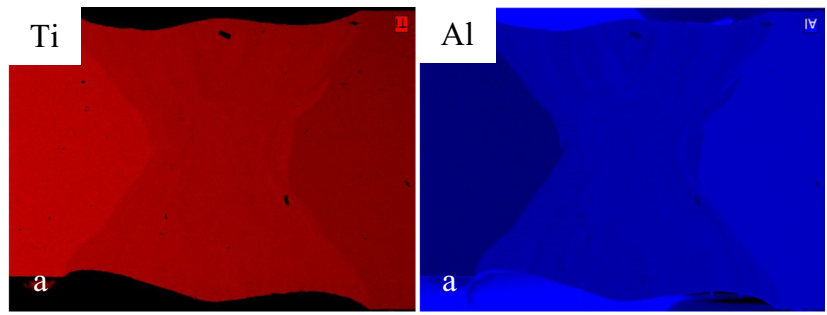
b



c

**Fig. 4** Optical micrographs of a T50A/TA6V, b T50A/21S, and c TA6V/21S ( $P = 3$  kW,  $v = 3$  m/min,  $\Delta x = 0$ ). The dotted line represents the initial joint plane [11]

**Fig. 5** EDX map of **a** T50A/TA6V, **b** 21S/T50A, and **c** TA6V/21S ( $P=3$  kW,  $v=3$  m/min, and  $\Delta x=0$  mm) [11]



material. The TA6V/21S couple displayed the best performances in terms of both elongation and strength. This heterogeneous combination managed to preserve the advantage of both alloys, i.e., higher strength resistance in comparison to the 21S and larger value of elongation to rupture in comparison to the TA6V. The shape of the stress-strain curve for the heterogeneous weld is nearly identical to that of the pure 21S.

About the welding conditions, we have noted that the higher the power and the lower the travel speed (i.e., the higher is the welding energy  $P/v$ ), the larger is the width of the bead regardless of the materials welded, as could be expected. The beam offset from the joint line is an important parameter in heterogeneous welding because of the different thermal conductivity of the materials (21.79, 6.60, and 7.60  $W m^{-1} K^{-1}$  for T50A, TA6V, and 21S, respectively (<http://www.matweb.com/>)). Nonetheless, the tests show that the welds prepared with  $\Delta x = 0$  mm displayed the best mechanical properties as shown in Fig. 2.

For all heterogeneous weld assemblies, the failure mostly took place away from the weld bead and in the material having the lowest strength. This result demonstrates the quality of the joints. Nevertheless, it should be noted that, for the TA6V/21S couple, the rupture of nearly 40% of the specimens occurred in the welded zone.

SEM observations of the fracture surface (Fig. 3a) revealed the presence of porosities, which are critical locations for strain concentration and crack initiation.

Therefore, these unexpected fractures could be explained by the presence of a few porosities of diameter up to 100  $\mu m$  as shown in the tomographic reconstruction (Fig. 3b) while porosities detected in the other couples were not as large (less than 30  $\mu m$ ).

An interesting fact is that these large pores are most of the time located close to the interface between the HAZ and the FZ, most often on the side of 21S. Recent work has been undertaken to understand the formation of porosities during laser welding. Residual gas analyses, conducted by Huang et al. [12] on Ti-6Al-4V sheets welded by electron beam, have shown that the gases retained in the porosities are mainly hydrogen and carbon dioxide. On the other hand, simulations performed by Pang et al. [13] suggested that during laser welding, the transient phenomenon of switching from conduction mode to keyhole mode was an important cause for instability of the vapor capillary. The results of their numerical simulations show that the oscillations of the melt facilitated the entry of the shielding gas into the keyhole causing an imbalance of the pressure that entrapped gas.

Porosities can be across the whole height of the bead but, in our experiments, they were mainly located towards the center. This phenomenon has already been observed and explained by Mohandas [14]. Two different physical aspects are the cause: the limit of gas solubility and the convective movements of the molten metal. The pores are principally the

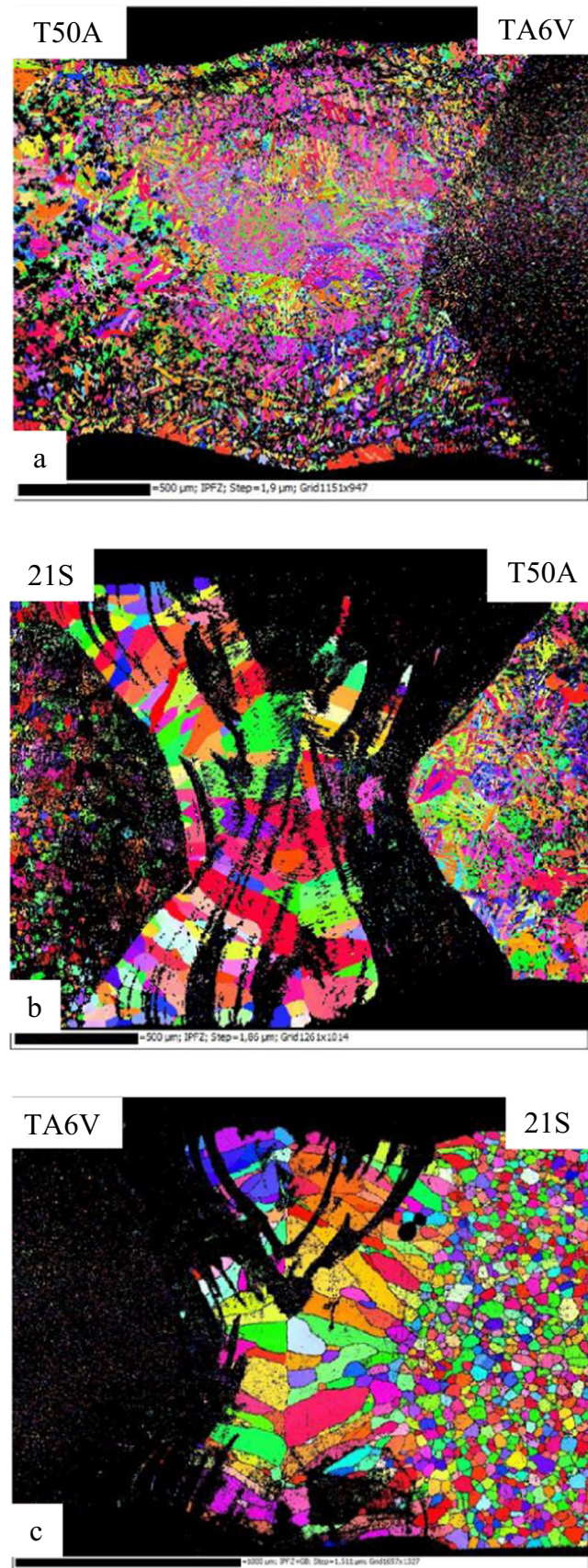


Fig. 6 EBSD map of a T50A/TA6V, b 21S/T50A, and c TA6V/21S ( $P = 3$  kW,  $v = 3$  m/min, and  $\Delta x = 0$  mm) [11]

**Table 2** Liquidus and solidus temperatures, and solidification ranges in equilibrium and with the Scheil model. Temperatures are given in degrees Celsius. Calculations made with Thermo-Calc and the TTTi3 database

Alloy	$T_{Liq}$	$T_{sol}$	$\Delta T(eq.)$	$\Delta T(Sch.)$
T50	1665	1655	10	80
TA6V	1704	1698	6	39
21S	1751	1725	26	91

consequence of the presence of hydrogen in the base metal (14–42 ppm). The gas solubility in the molten metal increases with the decrease of the temperature but drops abruptly at solidification. The bubble nucleation takes place at the fusion line, separating the molten metal from the surface of solid metal (HAZ). Hydrogen comes either from the solid or from the liquid center (where the temperature is higher so the diffusivity is higher) and the gathering of hydrogen led to the formation of bubbles. Depending on the conditions of dynamic convection and the solidification front speed for example, these bubbles can diffuse towards the surface and escape to the atmosphere. For electron beam or arc welding, the lower the travel speed of the source, the lower the porosity density because the bubbles have enough time to reach either the top or bottom surface of the FZ.

Results of our study indicated that the largest porosities were detected in couples containing 21S alloy. This is explained firstly by the fact that the solubility of hydrogen decreases with the amount of molybdenum and niobium as shown by Jones et al. [15]. Furthermore, the second proposed explanation is that, during the cooling, the highest value of viscosity of the weld pool is in these 21S-containing couples resulting from the presence of Mo and Nb alloying elements.

Consequently, we assumed that small bubbles formed but these are believed to travel only a short distance before coalescing and forming large bubbles. Their location can be explained by two possible ways: by nucleation and growth at the HAZ/FZ interface and by an easy migration along the solid wall. Further experiments and modeling should be undertaken to explain completely the formation of the porosities.

The as-received sheets presented equiaxed  $\alpha$  grains for T50A, equiaxed  $\beta$  grains for 21S, and inter-granular  $\beta$  phase in an equiaxed  $\alpha$  phase for TA6V alloy. Optical micrographs of the couples (Fig. 4) investigated in this study show different microstructures in the HAZ and FZ. For T50A-containing couple, the HAZ on the T50A side near the BM/HAZ interface presented very large  $\alpha$  grains, which changed into a mixture of  $\alpha$  and  $\alpha'$ . This alloy had the larger HAZ due to the high thermal conductivity. The HAZ on the TA6V side was found to be composed of a mixture of small  $\alpha$  and  $\alpha'$  grains in a  $\beta$  matrix, with the volume fraction of  $\alpha$  phase increasing as the distance from the FZ increased. The microstructure of the HAZ on the 21S side appeared to be similar to that of the base material because of the thermal stability of the  $\beta$  provided by the large concentration of  $\beta$ -stabilizer elements in this alloy.

In Fig. 4, the initial junctions between the heterogeneous titanium alloys are also indicated. Whereas for the T50A/TA6V couple, the initial and final junction line is more or less on the centerline of the formed FZ when the laser spot was not offset, the welds processed with the 21S alloy have an asymmetric FZ with more 21S being molten into the pool. This asymmetry during a heterogeneous welding is the cause of a combination of three physical properties: the difference in thermal conductivity, the difference in the reflectivity, and the difference in thermal expansion that moves the junction

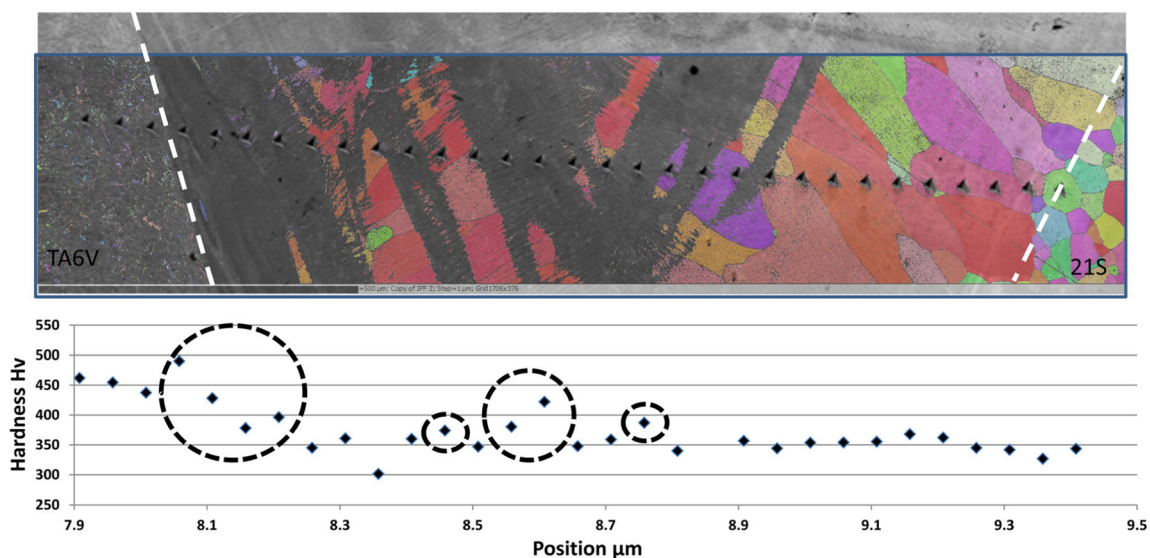


**Fig. 7** Vickers hardness obtained by nano-indentation across the bead of TA6V/21S ( $P = 3$  kW,  $v = 3$  m/min, and  $\Delta x = 0$  mm), corresponding EBSD map and SEM image. The molten zone borders are indicated with a white dotted line



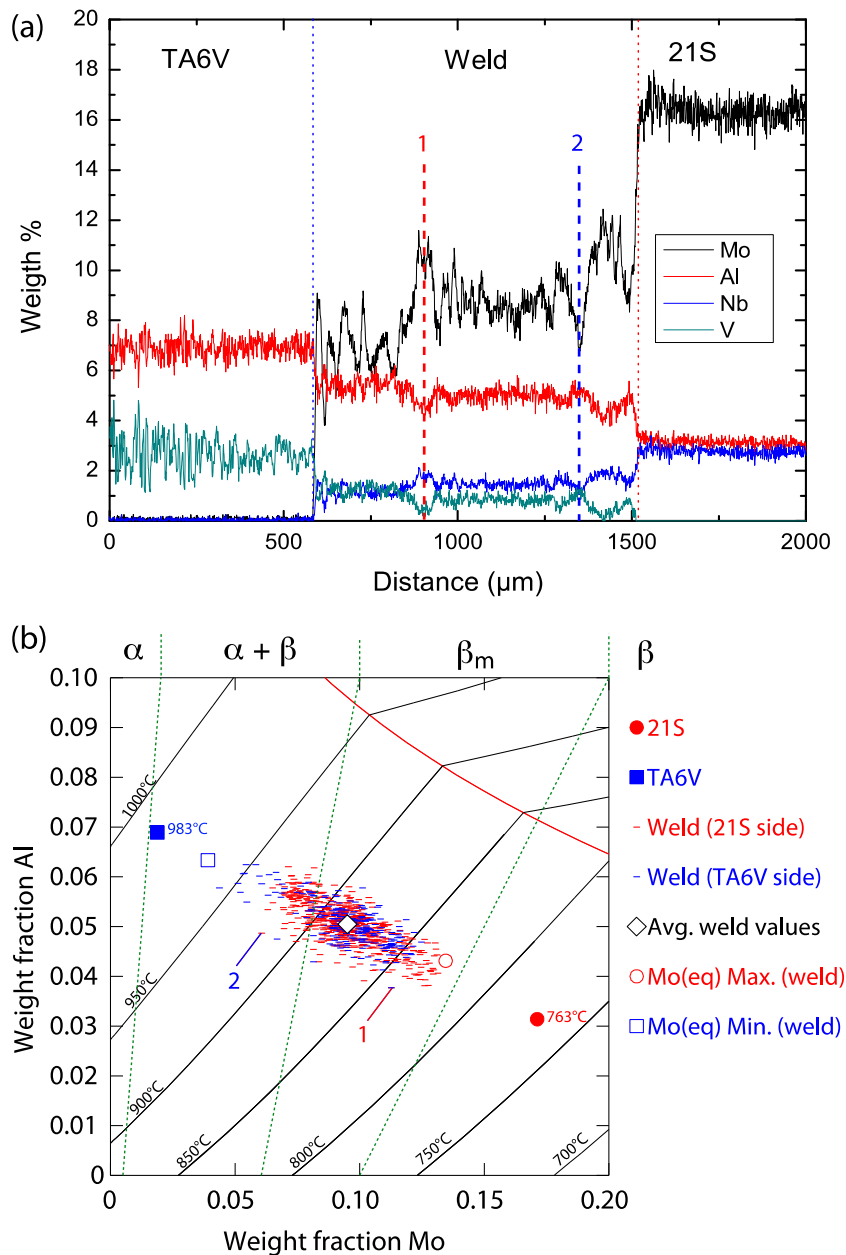
line. The FZ of the T50A/TA6V couple was found to be formed by acicular  $\alpha'$  grains resulting from the rapid cooling rate though the boundaries of the prior  $\beta$  grains are still clearly visible after etching. The 21S-containing couples kept very large  $\beta$  phase grains at room temperature due to its chemical composition. Moreover, in the case of the 21S alloy, the motion lines of the liquid bath could be detected in these micrographs.

EDX qualitative maps of the different couples are given in Fig. 5. The different alloys did not mix in the fusion zone, indicating that the inter-diffusion is weak, and this led to the formation of macro segregation bands. This observation is especially true for couples containing 21S. This phenomenon is believed to result from the consequence of the different

viscosities of the melts. This is confirmed by the presence of the heaviest elements of the couples at the bottom side of the weld bead. Note that the porosities are easily visible and do not seem to be in a particular chemical zone.

EBSD maps showing the grain morphology are given in Fig. 6. These maps are correlated with the EDX maps in Fig. 5. The first observation is that the  $\beta$  grains grow epitaxially from the HAZ to the center of the bead and thus form a clear central plane easily visible in Fig. 6c. As shown by the calculated values reported in Table 2, the various titanium alloys have similar liquidus temperatures. In addition, the solidification intervals are small, i.e., the largest value being equal to 91 °C for the 21S, as calculated with the Scheil model [16].

**Fig. 8** **a** Composition profiles across the weld for the TA6V/21S couple and **b**  $\beta$ -transus temperatures for the Ti-Mo-Al system superimposed with data from **a** expressed as aluminum and molybdenum equivalent [16]. The dashed lines indicate the frontier between the different types of Ti alloys (see text for details). The calculated  $\beta$ -transus temperatures for the two base alloys are also indicated



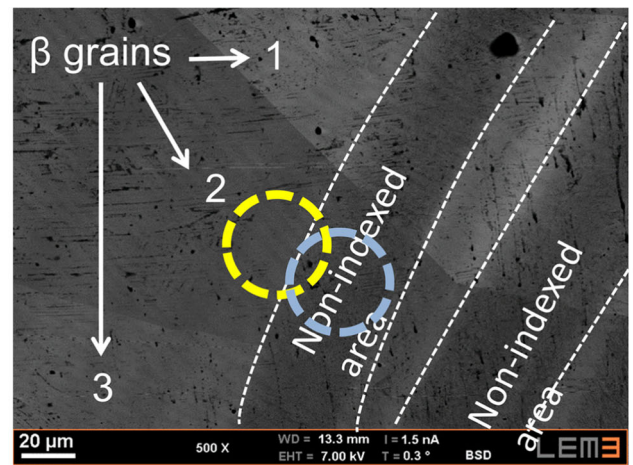
These two points show that for small solidification interval, the heat transfer that controls the solidification (rather than mass transfer) and, as a consequence, this heat transfer is similar in both materials, at least in the FZ. That is why the  $\beta$  grains have grown symmetrically in both parts of the FZ and met at the middle to form a vertical grain boundary.

Comparison of Figs. 5b, c and 6b, c shows that the non-indexed EBSD areas (black color) are those containing the larger concentration of  $\alpha$  stabilizer elements such as aluminum. We can note that, in the FZ of the 21S-containing couples, those areas are located on the side of the other alloy. Figure 7 shows the hardness evolution between the TA6V and the 21S alloys measured by nano-indentation. The comparison of the hardness with the EBSD map shows that the maximum hardness values correspond to non-indexed areas.

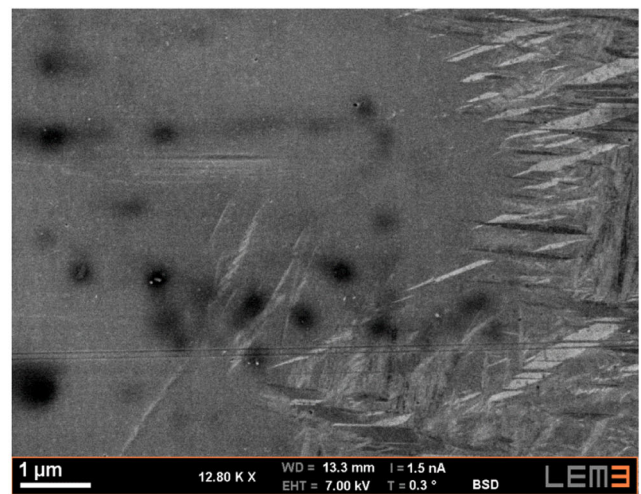
To understand this phenomenon, the chemical composition across the bead (and so across the macro segregation bands) of TA6V/21S was analyzed and the results are given in Fig. 8a. Point 1 corresponds to an indexed EBSD area and point 2 to a non-indexed one.

Figure 8b shows the evolution of the  $\beta$ -transus temperature with the Al and Mo content. For titanium alloys, it is possible to calculate the aluminum equivalent percentage for  $\alpha$  stabilizer alloying elements and the molybdenum equivalent percentage for  $\beta$  stabilizer elements [17]. The equivalent corresponding values for the profile in Fig. 8a were plotted in Fig. 8b. The  $\beta$ -transus temperatures of the two base alloys were also calculated and are indicated in Fig. 8b. Finally, the dashed lines indicate the transition between Ti alloy families, i.e.,  $\alpha$ ,  $\alpha + \beta$ , metastable  $\beta$ , and  $\beta$  alloys. Several observations can be made from this figure. First, the  $\beta$ -transus range from 825 to 960 °C in the weld represents an interval of 135 °C. Then, while from the average composition the weld belong to the metastable  $\beta$  alloy field, individual compositions are spread in between the TA6V  $\alpha + \beta$  field and the 21S  $\beta$  field. As can be seen from Fig. 8a, the changes in composition are very steep and occur over a few micrometers only, leading consequently to sharp changes in the phase transformation temperatures. In particular, when looking at point 2 in Fig. 8a, b, it can be seen that on the 21S side, the local composition is in the metastable  $\beta$  field with  $T_\beta = 850$  °C while point 2 is clearly in the  $\alpha + \beta$  field with a  $T_\beta = 924$  °C.

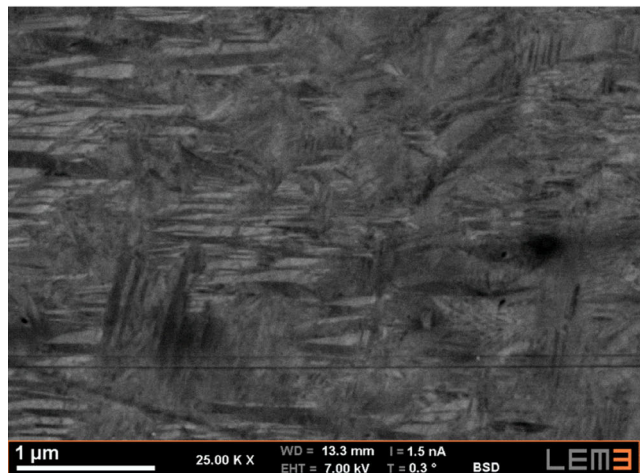
Figure 9a shows three large beta grains perfectly indexed with EBSD. These grains are separated by non-indexed bands, which have been outlined by the dotted lines in the figure. An observation under high magnification (Fig. 9b) on the border between both areas highlights the clear difference of the microstructure. The non-indexed areas are fully constituted by nanometric sized (Fig. 9c) and chaotic  $\alpha'$  needles formed during the rapid quenching underwent by the two-phase  $\alpha + \beta$  material. The continuity of the  $\beta$  grains across these non-indexed bands indicates that the chemical heterogeneities do not affect the solidification of the  $\beta$  grains, while their effect is



a



b



c

Fig. 9 SEM images of EBSD non-indexed area of TA6V/21S couple with **a** large area, **b** focus on the yellow circle, and **c** focus on the blue circle

much more pronounced at the solid state. The fact that the initial high-temperature microstructure is made of large  $\beta$  grains that have not yet experienced any solid-state transformation might play a role, since there are limited nucleation sites (grain boundaries, former sub-grain boundaries from the  $\alpha$  to  $\beta$  transformation upon heating, dislocations). Together with the high cooling rates associated with the welding process, this could lead to regions with few nucleation sites and a high transformation driving force that favors the martensitic transformation. Further studies are currently in progress to understand the formation of this nano-scale martensite.

## 4 Conclusion

To improve knowledge in the field of welding and more particularly for aeronautics, various heterogeneous titanium laser welds have been made using three different alloys: T50A, TA6V, and 21S. The experiments show four main points:

- Heterogeneous weld beads with T50A have the lower mechanical properties due to the martensitic transformation while the TA6V/21S displayed the best ultimate tensile strength.
- Our experience shows that one must be very careful during a heterogeneous weld with titanium alloys, especially when they contain a high molybdenum and niobium amount like the 21S. Indeed, the solubility of hydrogen decreases sharply with the presence of these elements and the gas bubbles thus formed are trapped in the FZ of high viscosity owing to  $\beta$  stabilizer alloys. These large porosities were detected near the HAZ/FZ interface.
- The 21S-containing couples gave large chemical segregations as a consequence of the alloying elements that possibly increased the viscosity of the molten zone.
- For the first time, it has been shown that these segregations cause the formation of nano-martensite in the areas rich in  $\alpha$  phase stabilizer elements. Other experiments should be done to verify the impact of this exotic microstructure on the corrosion resistance of the weld.

**Acknowledgments** The authors would like to thank Mélanie Duband (LICB) and Patrick Moll (LEM3) for their help during the experiments.

**Funding information** This research has been funded by the Laboratory of Excellence for Design of Alloy Metals for Low-mass Structures ('DAMAS' Labex).

## References

1. Chen YC, Nakata K (2009) Microstructural characterization and mechanical properties in friction stir welding of aluminum and titanium dissimilar alloys. *Mater Des* 30(3):469–474
2. Dressler U, Biallas G, Mercado UA (2009) Friction stir welding of titanium alloy TiAl6V4 to aluminium alloy AA2024-T3. *Mater Sci Eng A* 526(1–2):113–117
3. Kahramana N, Gülença B, Findik F (2005) Joining of titanium/stainless steel by explosive welding and effect on interface. *J Mater Process Technol* 169(2):127–133
4. Kamachi Mudali U et al (2003) Corrosion and microstructural aspects of dissimilar joints of titanium and type 304L stainless steel. *J Nucl Mater* 321(1):40–48
5. Borrisutthekul R, Miyashita Y, Mutoh Y (2005) Dissimilar material laser welding between magnesium alloy AZ31B and aluminum alloy A5052-O. *Sci Technol Adv Mater* 6(2):199–204
6. Gao M et al (2012) Laser keyhole welding of dissimilar Ti-6Al-4V titanium alloy to AZ31B magnesium alloy. *Metall Mater Trans A* 43(1):163–172
7. Wang SQ, Liu JH, Chen DL (2013) Tensile and fatigue properties of electron beam welded dissimilar joints between Ti-6Al-4V and BT9 titanium alloys. *Mater Sci Eng A* 584:47–56
8. Ferdinand C (2005) Mise en oeuvre et caractérisation d'assemblages soudés par procédés TIG et laser de tôles d'alliages de titane réfractaire (in French), PhD thesis, INPT, France
9. Oliver WC, Pharr GM (1992) An improved technique for determining hardness and elastic modulus using load and displacement sensing indentation experiments. *J Mater Res* 7(6):1564–1583
10. Andersson JO, Helander T, Höglund L, Shi PF, Sundman B (2002) Thermo-Calc and DICTRA, computational tools for materials science. *Calphad* 26(2):273–312
11. Weiss L et al. (2016) Microstructure and property of titanium heterogeneous laser welding. *Proceedings of the 13th World Conference on Titanium, TMS*, p 317–321
12. Huang JL et al (2012) On the mechanism of porosity formation during welding of titanium alloys. *Acta Mater* 60:3215–3225
13. Pang S, Chen W, Wang W (2014) A quantitative model of keyhole instability induced porosity in laser welding of titanium alloy. *Metall Mater Trans A* 45A:2808–2818
14. Mohandas T, Banerjee D, Kutumba Rao VV (1999) Fusion zone microstructure and porosity in electron beam welds of an  $\alpha + \beta$  titanium alloy. *Metall Mater Trans A* 30A:789–798
15. Jone DW, Pessall N, McQuillan AD (1961) Correlation between magnetic susceptibility and hydrogen solubility in alloys of early transition elements. *Philos Mag* 6(63):455–459
16. Scheil E (1942) Bemerkungen zur schichtkristallbildung. *Z Met* 34(3):70–72
17. Laheurte P (2003) Contribution à l'étude du comportement pseudo-élastique d'un alliage bêta métastable. Applications aux arcs orthodontiques (in French), Thesis, Université de Metz, France